

Electron tomography at 2.4-ångström resolution

M. C. Scott^{1*}, Chien-Chun Chen^{1*}, Matthew Mecklenburg^{1*}, Chun Zhu¹, Rui Xu¹, Peter Ercius², Ulrich Dahmen², B. C. Regan¹ & Jianwei Miao¹

Transmission electron microscopy is a powerful imaging tool that has found broad application in materials science, nanoscience and biology^{1–3}. With the introduction of aberration-corrected electron lenses, both the spatial resolution and the image quality in transmission electron microscopy have been significantly improved^{4,5} and resolution below 0.5 ångströms has been demonstrated⁶. To reveal the three-dimensional (3D) structure of thin samples, electron tomography is the method of choice^{7–11}, with cubic-nanometre resolution currently achievable^{10,11}. Discrete tomography has recently been used to generate a 3D atomic reconstruction of a silver nanoparticle two to three nanometres in diameter¹², but this statistical method assumes prior knowledge of the particle's lattice structure and requires that the atoms fit rigidly on that lattice. Here we report the experimental demonstration of a general electron tomography method that achieves atomic-scale resolution without initial assumptions about the sample structure. By combining a novel projection alignment and tomographic reconstruction method with scanning transmission electron microscopy, we have determined the 3D structure of an approximately ten-nanometre gold nanoparticle at 2.4-ångström resolution. Although we cannot definitively locate all of the atoms inside the nanoparticle, individual atoms are observed in some regions of the particle and several grains are identified in three dimensions. The 3D surface morphology and internal lattice structure revealed are consistent with a distorted icosahedral multiply twinned particle. We anticipate that this general method can be applied not only to determine the 3D structure of nanomaterials at atomic-scale resolution^{13–15}, but also to improve the spatial resolution and image quality in other tomography fields^{7,9,16–20}.

Since its introduction in 1968, electron tomography has been primarily used to determine the 3D structure of biological samples^{7,9}. In the past decade, electron tomography has been increasingly applied in materials science and nanoscience through the use of scanning transmission electron microscopy (STEM)^{8,10,11}. The highest resolution at present achieved by STEM tomography is around 1 nm in three dimensions^{10,11}, although slightly higher resolution has been obtained in a study of fullerene-like nanostructures with bright-field electron tomography²¹. A general electron tomography method with atomic-scale resolution, however, has not been demonstrated for several reasons. First, aligning the projections of a tomographic tilt series to a common axis with atomic level precision is technically challenging. Second, radiation damage limits the number of projections that can be acquired from a single object^{13,22}. Last, specimens cannot usually be tilted beyond $\pm 79^\circ$, preventing acquisition of data from the 'missing wedge'^{7–11}. Here we demonstrate that these limitations can be overcome or alleviated by applying a novel alignment approach and an iterative tomographic reconstruction method to a tilt series obtained via annular dark field (ADF)-STEM^{23,24}.

The conventional alignment approach used in electron tomography either relies on fiducial markers such as colloidal gold beads or is based on the cross-correlation between neighbouring projections^{7,9}. To our

knowledge, neither of these alignment approaches can achieve atomic-level precision. To overcome this limitation, we have developed a method based on the centre of mass, which is able to align the projections of a tilt series at atomic-level accuracy even with noise (Methods). To address the other two difficulties mentioned above, we have implemented a data acquisition and tomographic reconstruction method, termed equally sloped tomography^{16,18–20,25} (EST). Compared to conventional tomography, which reconstructs a 3D object from a tilt series of projections with constant angular increments, EST acquires a tilt series with equal slope increments, and then iterates back and forth between real and reciprocal space (Methods). In each iteration, constraints such as the sample boundary (that is, the support) and positivity of the Coulomb potential are applied in real space, while the measured projectional slices (that is, the Fourier transform of the projections) are enforced in reciprocal space. Each iteration is monitored by an error metric, and the algorithm is terminated after reaching a maximum number of iterations.

To test the feasibility of achieving a high-resolution tomographic reconstruction by the centre-of-mass and EST methods, we conducted numerical simulations on an ~ 5 -nm gold nanoparticle with icosahedral symmetry and a total of 3,871 atoms (Supplementary Figs 3a, 4a, c, e). A tilt series of 55 projections was obtained from the particle using multislice STEM calculations²⁶ (energy, 300 keV; spherical aberration, 1.2 mm; illumination semi-angle, 7.98 mrad; defocus, 48.6 nm; detector inner and outer angles, 13 and 78 mrad). To minimize nonlinear intensity contributions caused by dynamical scattering and electron channelling²⁷, projections along zone axis orientations were avoided. The tilt angles range from -72.6° to $+72.6^\circ$ with equal slope increments. To more closely approximate realistic experimental conditions, several additional modifications were made to generate the simulated data. First, the tilt angles were continuously shifted from 0° to 0.5° over the process of the tilt series and the magnification of the images was continuously changed from 0 to 0.2%. Second, each projection in the tilt series was arbitrarily shifted along the x and y axes, where the electron beam direction is parallel to the z axis. Last, Poisson noise was added to the projections of the tilt series with a total electron dose of $6.1 \times 10^6 \text{ e } \text{Å}^{-2}$. Supplementary Fig. 3 shows a linear projection of the model at 0° and the corresponding multislice STEM projection. The apparent increase of the atom size in the multislice projection was mainly caused by the nonlinear and diffraction effects in the nanoparticle.

The 55 projections were aligned to a common tilt axis with the centre-of-mass method, and were then reconstructed with the EST algorithm. Supplementary Fig. 4b, d, f shows three 2.5-Å-thick central slices of the 3D reconstruction in the x - y , z - x and z - y planes. Although the missing wedge problem is not completely solved (the top and bottom parts in Supplementary Fig. 4f) and the size of the reconstructed atoms is increased mainly due to the nonlinear and diffraction effects, the atomic positions and grain boundaries in the 3D reconstruction are consistent with the model. The simulation results indicate that the centre-of-mass and EST methods can be used

¹Department of Physics and Astronomy and California NanoSystems Institute, University of California, Los Angeles, California 90095, USA. ²National Center for Electron Microscopy, Lawrence Berkeley National Laboratory, Berkeley, California 94720, USA.

*These authors contributed equally to this work.

to achieve an atomic-scale resolution reconstruction from a tilt series of 55 projections with a missing wedge, nonlinear effects, Poisson noise and experimental errors.

Next, the centre-of-mass and EST methods were applied to experimental tilt series acquired from gold nanoparticles. Nanoparticles are an important class of materials with properties different from either molecules or bulk solids^{13–15}, and nano-gold is among the most widely studied of this class of material owing to its broad applications in chemistry, biology, materials science, nanoscience and nanotechnology²⁸. In this study, we imaged gold particles with a diameter of ~ 10 nm because smaller particles are not as stable under an electron beam^{13,22}. To reduce the electron dose, we used a low-exposure data acquisition scheme with a 300-keV ADF-STEM (Methods). When focusing an image, a nearby nanoparticle was first viewed (not the particle of interest), thus reducing the unnecessary radiation dose to the particle under study. Using this scheme, we acquired several tomographic tilt series of gold nanoparticles. Supplementary Fig. 5 shows a tilt series of 69 projections and their Fourier transforms, with a total electron dose of $\sim 7.6 \times 10^6 \text{ e} \text{ \AA}^{-2}$. Supplementary Fig. 6 shows three 0° projections and their Fourier transforms measured during the acquisition of this tilt series to monitor the effects of radiation damage. Although some minor shape changes occurred, the crystal lattice structure of the particle remained consistent throughout the experiment.

To investigate the nonlinear effects in the experiment, we simulated an ~ 10 -nm gold particle with icosahedral symmetry and performed multislice STEM calculations on an 11.5- \AA -thick slab of this particle²⁶ (Supplementary Fig. 7). Although the atom size was increased, mainly owing to the nonlinear diffraction and dynamical scattering effects, the multislice STEM projection exhibits a crystal lattice structure consistent with the model. We then calculated a tilt series for a 2.5- \AA central slice using the multislice simulations. The tilt series consists of 69 projections with a tilt range of $\pm 72.6^\circ$. Supplementary Fig. 8 shows the model and reconstructed slices. The atomic positions and the

internal grain boundaries are resolved, except in a very few places owing to the nonlinear effects in the projections.

After investigating the nonlinear effects, we performed post data analysis of the experimental tilt series (Methods), and aligned the projections with the centre-of-mass method. To reconstruct the 3D structure, we first estimated a loose 3D support, defined to be larger than the particle boundary. After 500 iterations of the EST algorithm, the reconstruction was used to determine a tight support (that is, close to the true boundary of the particle). Using the tight support, we ran another 500 iterations and obtained a final 3D structure. To examine the quality of the reconstruction, we calculated 69 projections from the final 3D structure and found the average normalized discrepancy with the measured projections to be 6.7% (Supplementary Methods and Supplementary Table 1). Representative measured and calculated projections at different particle orientations are shown in Fig. 1 and Supplementary Fig. 9. Although there are some minor differences between the two projections, the overall shape and lattice structure agree well. To more rigorously examine the accuracy of the reconstruction, an EST reconstruction was performed from 68 experimental projections by removing the 7.1° projection. The 3D reconstruction was then projected back to calculate the projection at 7.1° , which is consistent with the experimentally measured one (Supplementary Fig. 10).

To estimate the resolution achieved in the reconstruction, we chose a 3.36- \AA -thick central slice in the x - y plane. Figure 2a, b shows the slice and its Fourier transform, in which the distance between two neighbouring atom columns and the location of the Bragg peaks indicate that a resolution of 2.4 \AA was achieved in the x and y directions. To estimate the resolution along the z axis (beam direction), we selected a 3.36- \AA -thick slice with the horizontal axis along the z axis (Fig. 2c, d). The resolution close to the z axis was determined to be 2.4 \AA . Individual atoms are visible in some regions of the slices, but not all atoms can be identified in the slices. Supplementary Fig. 11 shows two 3.36- \AA -thick slices of the nanoparticle in a different orientation,

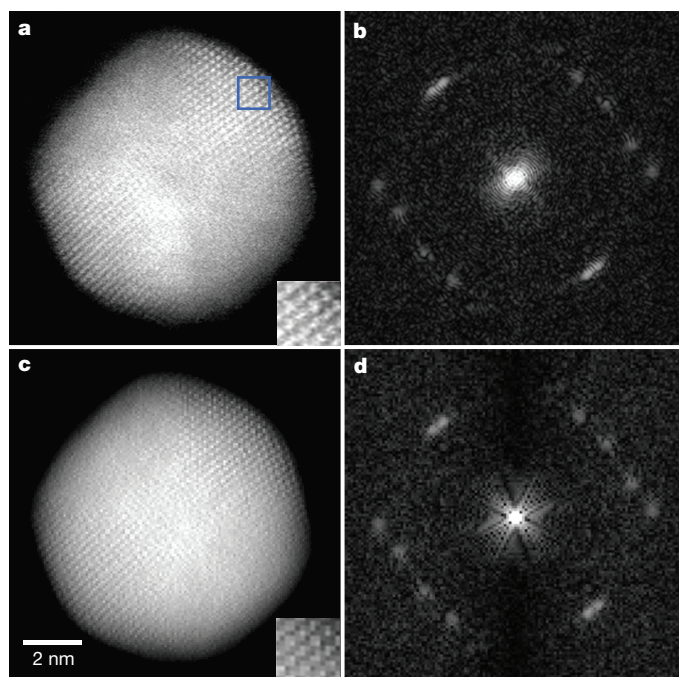


Figure 1 | Evaluation of the 3D reconstruction quality. **a–d**, Representative measured (**a**) and calculated (**c**) projections and their Fourier transforms (respectively **b**, **d**) at tilt angle 7.1° . Insets in **a** and **c** show the projected atomic positions inside the blue square in the main panel. The overall shape of the nanoparticle and the location of the Bragg peaks agree well, indicating a good quality 3D reconstruction. This gold nanoparticle is the same as studied in Figs 2–4.

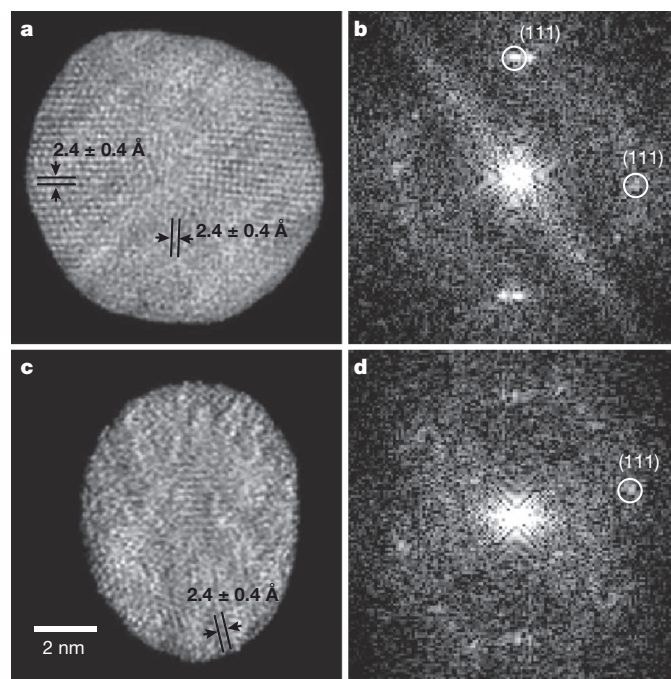


Figure 2 | Estimation of the 3D resolution of the reconstruction of the gold nanoparticle. **a**, **b**, A 3.36- \AA thick central slice in the x - y plane (**a**) and its Fourier transform (**b**), indicating that a resolution of 2.4 \AA corresponding to the gold (111) lattice was achieved along the x and y axes. **c**, **d**, A 3.36- \AA -thick slice in the z - y plane (**c**) and its Fourier transform (**d**) where the horizontal axis is along the z axis (beam direction). The resolution in the z axis was estimated to be 2.4 \AA . Individual atoms are visible in some regions of the slices, but not all atoms can be identified in the slices.

exhibiting crystal lattice structure that is not present in Fig. 2a and c. The apparent flattening of the particle along the beam axis was also observed in the 3D reconstructions (Fig. 2 and Supplementary Movie 1), and was probably caused by the interaction between the nanoparticle and the Si substrate.

To visualize the internal structure and the morphology of the gold nanoparticle, we generated 3D volume and iso-surface renderings of the reconstruction, in which both surface and internal lattice structures are visible (Supplementary Movies 1 and 2). Figure 3a, b shows volume renderings of the nanoparticle and their Fourier transforms (insets) at the two- and three-fold symmetry orientations. The corresponding iso-surface renderings at the same orientations are shown in Fig. 3c and d. The overall 3D shape and facets of the nanoparticle are consistent with an icosahedron (insets in Fig. 3c and d). To identify internal 3D grains, we applied the 3D Fourier transform to the reconstruction. By identifying the Bragg peaks of each major grain and applying the 3D inverse Fourier transform to the selected Bragg peaks, we determined four major 3D grains inside the gold nanoparticle (Methods). Figure 4 and Supplementary Movie 3 show a volume rendering of the four grains in three dimensions, in which grains 1, 2 and grains 3, 4 are related by mirror-reflection across the horizontal interfaces marked by dotted lines. The angle enclosed by close-packed planes across these interfaces was measured to be $69.9^\circ \pm 0.8^\circ$ between grains 1 and 2, and $71.3^\circ \pm 0.8^\circ$ between grains 3 and 4, both of which are consistent with the angle for a face-centred-cubic twin boundary (70.53°). By applying the same method to some other Bragg peaks, we identified 3D grains in the top and bottom parts of the particle (Supplementary Fig. 12). The surface morphology and the internal lattice structures suggest that this is a distorted icosahedral multiply twinned particle, typically found for nano-gold in the size range above 10 nm (ref. 29).

By combining the centre-of-mass alignment technique and the EST reconstruction method with an ADF-STEM, we have determined the 3D structure of a ~ 10 -nm gold nanoparticle at 2.4 Å resolution from a tilt series of 69 projections with a missing wedge. Several grains are identified inside the nanoparticle in three dimensions. Although individual

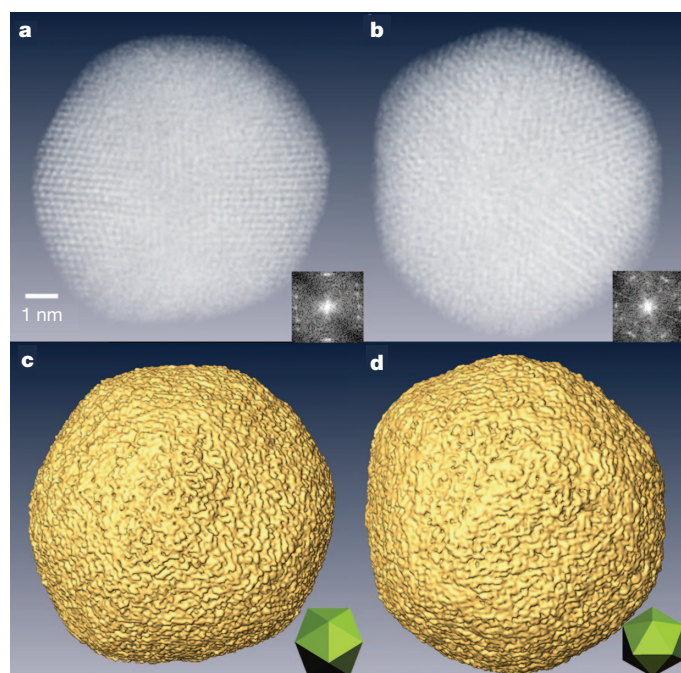


Figure 3 | 3D structure of the reconstructed gold nanoparticle. **a, b**, 3D volume renderings of the nanoparticle and their Fourier transforms (insets) at the two-fold (**a**) and three-fold (**b**) symmetry orientations. **c, d**, Iso-surface renderings of the nanoparticle at the two-fold (**c**) and three-fold (**d**) symmetry orientations. Insets show a model icosahedron at the same orientations.

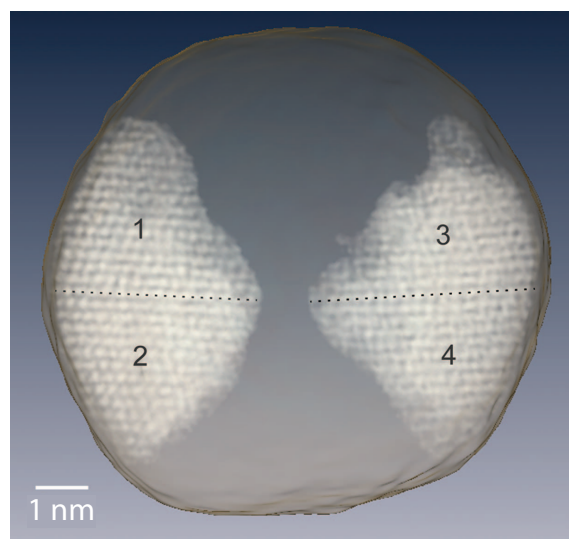


Figure 4 | Identification of four major grains inside the gold nanoparticle in three dimensions. Grains 1, 2 and grains 3, 4 are related by mirror-reflection across the horizontal interfaces marked by dotted lines. The angle enclosed by close-packed planes across these interfaces was measured to be $69.9^\circ \pm 0.8^\circ$ between grains 1 and 2, and $71.3^\circ \pm 0.8^\circ$ between grains 3 and 4, both of which are consistent with the angle for a face-centred cubic twin boundary (70.53°).

atoms are visible in some regions of the nanoparticle, we cannot definitively locate all of the atoms inside the particle. In order to identify all the atoms in the particle (estimated to be $\sim 23,800$) without using atomicity and bond information, a resolution higher than 2.4 Å is needed, which requires future developments. With aberration-corrected STEM^{4,23,24}, better 3D resolution and image quality should be achievable, but extended depth-of-field techniques may have to be applied to the tilt series before the EST reconstruction can be performed. Compared to atom-probe tomography³⁰, this non-destructive technique can not only handle isolated nanoparticles, but also provide the 3D local structure of complex nanomaterials at high resolution.

METHODS SUMMARY

Gold nanoparticles with a size of ~ 10 nm (Ted Pella) were supported on 5-nm-thick Si membranes (TEMwindows.com), which can withstand plasma cleaning for a longer period than carbon substrates to alleviate carbon contamination. Tomographic tilt series with equal slope increments were acquired from the gold nanoparticles by using an ADF-STEM (FEI Titan 80-300). The tilt angles (θ) were determined by^{16,25} $\theta = -\tan^{-1}[(N+2-2n)/N]$ for $n = 1, \dots, N$ and $\theta = \pi/2 - \tan^{-1}[(3N+2-2n)/N]$ for $n = N+1, \dots, 2N$ with $N = 32$ or 64 in this experiment. The angles beyond $\pm 72.6^\circ$ were not accessible owing to the geometry of the support grid. To monitor the radiation induced stability effect, several projections at the same particle orientation were measured during the acquisition of each tilt series (Supplementary Fig. 6). To improve the 3D reconstruction and enhance the signal to noise ratio, the background of the projections was subtracted and 2×2 pixel binning was performed for each projection. After post data analysis, the tilt series was aligned with the centre-of-mass method (Methods). The reconstruction of the aligned tilt series was conducted using the EST method, which iterated back and forth between real and reciprocal space with constraints enforced in real space and measured data in reciprocal space (Methods, Supplementary Methods and Supplementary Fig. 2). To examine the reconstruction quality, the reconstructed 3D structure was projected back to obtain 69 projections, which were compared to the corresponding measured ones. An average R_{real} (Supplementary Methods) was calculated to be 6.7%, indicating a good quality reconstruction (Fig. 1, Supplementary Table 1).

Full Methods and any associated references are available in the online version of the paper at www.nature.com/nature.

Received 18 April 2011; accepted 9 February 2012.

- Williams, D. B. & Carter, C. B. *Transmission Electron Microscopy: A Textbook for Materials Science* 2nd edn (Springer, 2009).

2. Spence, J. C. H. *Experimental High-Resolution Electron Microscopy* 3rd edn (Oxford Univ. Press, 2003).
3. Frank, J. *Three-Dimensional Electron Microscopy of Macromolecular Assemblies* (Oxford Univ. Press, 2006).
4. Batson, P. E., Dellby, N. & Krivanek, O. L. Sub-ångström resolution using aberration corrected electron optics. *Nature* **418**, 617–620 (2002).
5. Haider, M. *et al.* Electron microscopy image enhanced. *Nature* **392**, 768–769 (1998).
6. Erni, R., Rossell, M. D., Kisielowski, C. & Dahmen, U. Atomic-resolution imaging with a sub-50-pm electron probe. *Phys. Rev. Lett.* **102**, 096101 (2009).
7. Frank, J. *Electron Tomography* (Plenum, 1992).
8. Midgley, P. A. & Weyland, M. 3D electron microscopy in the physical sciences: the development of Z-contrast and EFTEM tomography. *Ultramicroscopy* **96**, 413–431 (2003).
9. Lučić, V., Förster, F. & Baumeister, W. Structural studies by electron tomography: from cells to molecules. *Annu. Rev. Biochem.* **74**, 833–865 (2005).
10. Midgley, P. A. & Dunin-Borkowski, R. E. Electron tomography and holography in materials science. *Nature Mater.* **8**, 271–280 (2009).
11. Arslan, I., Yates, T. J. V., Browning, N. D. & Midgley, P. A. Embedded nanostructures revealed in three dimensions. *Science* **309**, 2195–2198 (2005).
12. Van Aert, S., Batenburg, K. J., Rossell, M. D., Erni, R. & Van Tendeloo, G. Three-dimensional atomic imaging of crystalline nanoparticles. *Nature* **470**, 374–377 (2011).
13. Marks, L. D. Experimental studies of small particle structures. *Rep. Prog. Phys.* **57**, 603–649 (1994).
14. Billinge, S. J. L. & Levin, I. The problem with determining atomic structure at the nanoscale. *Science* **316**, 561–565 (2007).
15. Yacamán, M. J., Ascencio, J. A., Liu, H. B. & Gardea-Torresdey, J. Structure shape and stability of nanometric sized particles. *J. Vac. Sci. Technol. B* **19**, 1091–1023 (2001).
16. Lee, E. *et al.* Radiation dose reduction and image enhancement in biological imaging through equally sloped tomography. *J. Struct. Biol.* **164**, 221–227 (2008).
17. Kak, A. C. & Slaney, M. *Principles of Computerized Tomographic Imaging* (SIAM, Philadelphia, 2001).
18. Fahimian, B. P., Mao, Y., Cloetens, P. & Miao, J. Low dose X-ray phase-contrast and absorption CT using equally-sloped tomography. *Phys. Med. Biol.* **55**, 5383–5400 (2010).
19. Mao, Y., Fahimian, B. P., Osher, S. J. & Miao, J. Development and optimization of regularized tomographic reconstruction algorithms utilizing equally-sloped tomography. *IEEE Trans. Image Process.* **19**, 1259–1268 (2010).
20. Jiang, H. *et al.* Quantitative 3D imaging of whole, unstained cells by using X-ray diffraction microscopy. *Proc. Natl Acad. Sci. USA* **107**, 11234–11239 (2010).
21. Bar Sadan, M. *et al.* Toward atomic-scale bright-field electron tomography for the study of fullerene-like nanostructures. *Nano Lett.* **8**, 891–896 (2008).
22. Bovin, J.-O., Wallenberg, R. & Smith, D. J. Imaging of atomic clouds outside the surfaces of gold crystals by electron microscopy. *Nature* **317**, 47–49 (1985).
23. Muller, D. A. Structure and bonding at the atomic scale by scanning transmission electron microscopy. *Nature Mater.* **8**, 263–270 (2009).
24. Pennycook, S. J. & Nellist, P. D. *Scanning Transmission Electron Microscopy: Imaging and Analysis* 1st edn (Springer, 2011).
25. Miao, J., Förster, F. & Levi, O. Equally sloped tomography with oversampling reconstruction. *Phys. Rev. B* **72**, 052103 (2005).
26. Kirkland, E. J. *Advanced Computing in Electron Microscopy* 2nd edn (Springer, 2010).
27. Howie, A. Diffraction channelling of fast electrons and positrons in crystals. *Phil. Mag.* **14**, 223–237 (1966).
28. Daniel, M. C. & Astruc, D. Gold nanoparticles: assembly, supramolecular chemistry, quantum-size-related properties, and applications toward biology, catalysis, and nanotechnology. *Chem. Rev.* **104**, 293–346 (2004).
29. Barnard, A. S., Young, N. P., Kirkland, A. I., van Huis, M. A. & Xu, H. Nanogold: a quantitative phase map. *ACS Nano* **3**, 1431–1436 (2009).
30. Arslan, I., Marquis, E. A., Homer, M., Hekmaty, M. & Bartelt, N. C. Towards better 3-D reconstructions by combining electron tomography and atom-probe tomography. *Ultramicroscopy* **108**, 1579–1585 (2008).

Supplementary Information is linked to the online version of the paper at www.nature.com/nature.

Acknowledgements We thank E. J. Kirkland for help with multislice STEM calculations, R. F. Egerton, Z. H. Zhou and J. A. Rodríguez for discussions and I. Atanasov for assistance in data acquisition. The tomographic tilt series were acquired at the Electron Imaging Center for NanoMachines of the California NanoSystems Institute. This work was partially supported by UC Discovery/TomoSoft Technologies (IT107-10166).

Author Contributions J.M. conceived the overall project; M.C.S., M.M., C.Z., B.C.R. and J.M. designed and conducted the experiments; C.Z., R.X., C.-C.C., P.E. and J.M. did multislice STEM calculations; C.-C.C. and J.M. performed the data analysis and image reconstruction; U.D., J.M., C.-C.C., M.C.S., M.M. and B.C.R. interpreted the results, and J.M., M.C.S., C.-C.C. and M.M. wrote the manuscript. All authors commented on the manuscript.

Author Information Reprints and permissions information is available at www.nature.com/reprints. The authors declare no competing financial interests. Readers are welcome to comment on the online version of this article at www.nature.com/nature. Correspondence and requests for materials should be addressed to J.M. (miao@physics.ucla.edu).

METHODS

Sample preparation. Gold nanoparticle solution with an average particle size of ~ 10 nm (Ted Pella) was sonicated for ~ 10 min to prevent aggregation. Five-nm-thick Si membranes (TEMwindows.com) were used as the particle substrates in the experiment. The thin membrane, with a size of $100 \times 1,500 \mu\text{m}$, is supported on a $100\text{-}\mu\text{m}$ -thick Si frame, allowing for a maximum tilt range of $\pm 83^\circ$. To avoid breaking the membrane, a micromanipulator was used to place a small drop of solution onto the outer frame of the Si grid. After gently moving the drop onto the membrane, it was removed and not allowed to dry and leave excessive gold particles and contaminants. The Si grids were cleaned pre-deposition in a Gatan Solarus plasma cleaner (Model 950) for 20 s using a standard H_2/O_2 recipe. To further ensure removal of contaminant sources, the sample holder (Fischione Model 2020) was plasma-cleaned for an hour before data acquisition using the same recipe.

ADF-STEM. STEM images of gold nanoparticles were acquired on a FEI Titan 80-300 (energy, 300 keV; spherical aberration, 1.2 mm; illumination semi-angle, 7.98 mrad; and defocus, 48.6 nm). The 70 pA electron beam was focused to a probe with a $50 \mu\text{m}$ probe-forming aperture (C2) and rastered over the sample. The scattered electrons were captured by a Fischione Model 3000 ADF detector with angles between 13 mrad and 78 mrad from the optical axis. The use of ADF angles was to improve the signal to noise ratio with a low current electron beam. The effects of nonlinear image intensities and diffraction contrast were carefully determined by multi-slice simulations. The maximum tilt angles were limited by the holder to $\pm 75^\circ$.

Low-exposure acquisition of tomographic tilt series. In order to reduce vibration and drift during data acquisition, the sample holder was allowed to settle for one hour after insertion into the microscope, and also for several minutes after moving to each new angle. Tilt series were acquired by manually changing the angle with equal slope increments. The tilt angles (θ) were determined by $\theta = -\tan^{-1}[(N+2-2n)/N]$ for $n = 1, \dots, N$ and $\theta = \pi/2 - \tan^{-1}[(3N+2-2n)/N]$ for $n = N+1, \dots, 2N$ with $N = 32$ or 64 in this experiment. To focus each projectional image during data acquisition, a nearby particle was used (rather than the particle of interest) to reduce the radiation dose to the particle. By using this low-exposure data acquisition scheme, we have obtained several tomographic tilt series. Supplementary Fig. 5 shows the tilt series used in this reconstruction with 69 projections and a tilt range of $\pm 72.6^\circ$. A representative sinogram of the tilt series is shown in Supplementary Fig. 13. The probe current was ~ 70 pA with a dwell time of $45 \mu\text{s}$ per pixel, and the magnification of each projection was 5.2×10^6 . Since the pixel size in STEM mode can vary, a calibration image of the particle was taken in TEM mode, and the STEM pixel size was determined to be 0.42 \AA . The total electron dose of the tilt series was estimated to be $\sim 7.6 \times 10^6 \text{ e} \text{ \AA}^{-2}$. Supplementary Fig. 6 shows three 0° projections measured during the acquisition of this tilt series. Although some minor shape changes occurred, the crystal lattices of the particle remained consistent throughout the experiment.

Post data analysis. In order to apply the EST method, the background surrounding the nanoparticle in each projection has to be subtracted. To systematically eliminate the background, we first projected all the projections onto the tilt axis and obtained a set of 1D curves. We then determined the optimal cut-off value for background subtraction in each projection by maximizing the cross-correlation among these 1D curves. After background subtraction, we binned 2×2 pixels into 1 pixel, which was used to enhance the signal to noise ratio in the projections and improve the EST reconstruction. The background subtracted and binned projections with pixel size of 0.84 \AA were aligned using the centre-of-mass approach and reconstructed with the EST method.

The centre-of-mass alignment method. To achieve an atomic scale resolution reconstruction, the projections in a tilt series have to be aligned to a common axis (not necessarily the true tilt axis) with atomic level precision in both the x and y axes, where the y axis represents the tilt axis and the z axis the beam direction. To align the tilt series along the y axis, the projections were first projected onto the y axis and a set of 1D curves was generated. We then chose a 1D curve at 0° as a reference, and aligned the remaining curves to the reference. To align the projections along the x axis, we developed a method based on the centre of mass. When a 3D object is tilted around the y axis from 0° to 360° , the centre-of-mass of the object forms a circle. However, in the special geometry where the centre of mass coincides with the origin of the x axis, this circle becomes a point. To determine the centre of mass in this special geometry, we projected each 2D projection onto the x axis, chose a pixel as the origin and calculated the centre of mass (CM) along the x axis, $x_{\text{CM}} = \sum_i x_i \rho(x_i) / \sum_i \rho(x_i)$, where $\rho(x_i)$ is the Coulomb potential at position x_i . We then shifted this projection to set x_{CM} as the new origin of the x axis. Through repeating this process for all projections, we aligned the tilt series to the common axis that coincides with the new origin. Both our simulation and experimental results indicate that the centre-of-mass alignment is a general method and can align the projections of a tilt series at atomic level accuracy, even

with relatively high noise and the nonlinear effects (Fig. 1, Supplementary Figs 4 and 8, and Supplementary Table 1).

The EST method. When the projections of a tilt series use equal slope increments, it has been shown that a direct fast Fourier transform, the pseudopolar fast Fourier transform (PPFFT)³¹, exists between a pseudopolar grid and a Cartesian grid. Supplementary Fig. 1 shows a pseudopolar grid and the PPFFT. For an $N \times N$ Cartesian grid, the corresponding pseudopolar grid is defined by a set of $2N$ lines, each line consisting of $2N$ grid points mapped out on N concentric squares. The $2N$ lines are subdivided into a horizontal group (in blue) defined by $y = sx$, where s is the slope and $|s| \leq 1$, and a vertical group (in red) defined by $x = sy$, where $|s| \leq 1$; the horizontal and vertical groups are symmetric under the interchange of x and y , and $\Delta s = 2/N$. When these conditions are met, the PPFFT and its inverse algorithm are mathematically faithful³¹. Note that the PPFFT and its inverse algorithm were originally developed to interpolate tomographic projections from a polar to a Cartesian grid in reciprocal space. The idea of acquiring tomographic tilt-series at equal slope increments and then combining the PPFFT with iterative algorithms for 3D image reconstructions was first suggested in 2005 (ref. 25).

Compared to other data acquisition approaches, such as the Saxton scheme³², the EST data acquisition approach is different in that it acquires projections with equal slope increments in order to use the PPFFT. Although the PPFFT and its inverse provide an algebraically faithful way to do the fast Fourier transform between the Cartesian and pseudopolar grids, three difficulties limit its direct application to electron tomography. First, the tilt range has to be from -90° to $+90^\circ$. Second, the number of projections in a tilt series needs to be $2N$ for an $N \times N$ object. Third, the grid points past the resolution circle (dashed circle in Supplementary Fig. 1) cannot be experimentally determined. We overcame these limitations by combining the PPFFT with an iterative process^{16,18–20,25}. Supplementary Fig. 2 shows the schematic layout of the iterative EST method. We first convert the electron micrograph projections to Fourier slices in the pseudopolar grid. As illustrated in Supplementary Fig. 1, the distance between the sampling points on the individual $2N$ lines of the pseudopolar grid varies from line to line. In order to calculate the Fourier slices from the projections, the fractional Fourier transform is used to vary the output sampling distance of the Fourier slices³³. By applying the inverse PPFFT, we obtain a 3D image in real space. A 3D support is defined to separate the object from a zero region where the size of the zero region is proportional to the over-sampling of the projections³⁴. The negative-valued voxels inside the support and the voxel values outside the support are set to zero, and a new 3D image is obtained. The forward PPFFT is applied to the new image and a set of calculated Fourier slices is obtained. We then replace the corresponding calculated Fourier slices with the measured ones, and the remaining slices are kept unchanged. The iterative process is then repeated with each iteration monitored by an R_{recip} (Supplementary Methods). The algorithm is terminated after reaching a maximum number of iterations. A more detailed description of the EST method is presented in Supplementary Methods. Compared to phase retrieval in coherent X-ray/electron diffraction imaging^{20,35–37}, the EST method aims to solve the missing data by combining an iteration process with the PPFFT algorithm.

Identification of the major 3D grains inside the nanoparticle. The following procedures were used to determine the major 3D grains inside the gold nanoparticle. (1) Apply the 3D Fourier transform to the reconstructed nanoparticle and identify the Bragg peaks corresponding to a major grain. (2) Use small spheres with soft edges to select these Bragg peaks and set other values to zero. (3) Apply the 3D inverse Fourier transform to the selected Bragg peaks and obtain a 3D image. (4) Convolve the 3D image with a Gaussian filter and choose a cut-off value to determine the 3D shape of the grain. (5) Use the 3D shape to identify the corresponding 3D grain in the reconstructed nanoparticle. (6) Repeat steps 1–5 to determine other major grains.

1. Averbuch, A., Coifman, R. R., Donoho, D. L., Israeli, M. & Shkolnisky, Y. A framework for discrete integral transformations I — the pseudopolar Fourier transform. *SIAM J. Sci. Comput.* **30**, 785–803 (2008).
2. Saxton, W. O., Baumeister, W. & Hahn, M. Three-dimensional reconstruction of imperfect two-dimensional crystals. *Ultramicroscopy* **13**, 57–70 (1984).
3. Bailey, D. H. & Swartztrauber, P. N. The fractional Fourier transform and applications. *SIAM Rev.* **33**, 389–404 (1991).
4. Miao, J., Sayre, D. & Chapman, H. N. Phase retrieval from the magnitude of the Fourier transform of non-periodic objects. *J. Opt. Soc. Am. A* **15**, 1662–1669 (1998).
5. Miao, J., Charalambous, P., Kirz, J. & Sayre, D. Extending the methodology of X-ray crystallography to allow imaging of micrometre-sized non-crystalline specimens. *Nature* **400**, 342–344 (1999).
6. Miao, J., Ohshima, T., Terasaki, O., Hodgson, K. O. & O’Keefe, M. A. Atomic resolution three-dimensional electron diffraction microscopy. *Phys. Rev. Lett.* **89**, 155502 (2002).
7. Zuo, J. M., Vartanyants, I., Gao, M., Zhang, R. & Nagahara, L. A. Atomic resolution imaging of a carbon nanotube from diffraction intensities. *Science* **300**, 1419–1421 (2003).